COMSOL
CONFERENCE
2025 AMSTERDAM

A Multiphysics Model of Lymph Node Hydraulics and Solute Transport with RTD-Based Validation

R. Kandhai[1], J. Bridge[2]
1,2. Department of Mechanical and Manufacturing Engineering, The University of the West Indies, St Augustine Campus, Trinidad and Tobago.

Abstract

Lymph nodes regulate immune surveillance and lymph transport, yet node-scale hydraulics and solute residence times are difficult to measure in vivo. A 2D axisymmetric Stokes–Darcy–poroelastic model in COMSOL Multiphysics couples free-fluid flow in the subcapsular and medullary sinuses with porous parenchymal transport and solid deformation, linked to advection–diffusion of a passive solute. A residence-time distribution (RTD) analysis of a short tracer pulse calibrates medullary permeability and validates node-scale pressure drops. Under physiologic inflow and efferent outlet pressure, the calibrated model reproduces a pressure drop of ~1 mmHg, predicts dominant peripheral shunting (~99.9%) with limited core perfusion, capsule wall shear stresses on the order of 0.1–2 Pa, and a mean RTD of ~4 h with a long tail reflecting parenchymal exchange and retention. The framework yields quantitative, interpretable metrics including Δp, shear, flow partitioning, and RTD that are useful for comparing geometries and operating conditions and for assessing therapeutic strategies that depend on lymph borne delivery. The platform is readily extensible to chemokine-guided immune-cell transport and spatial heterogeneity, enabling more mechanistic studies of lymph node function in health and disease.

Keywords: Lymph node; Darcy–Stokes coupling; Poroelasticity; Free and porous media flow; Residence-time distribution (RTD); Solute transport; COMSOL Multiphysics.

Introduction

Lymph nodes (LNs) are secondary lymphoid organs that integrate interstitial fluid drainage with immune surveillance, coordinating antigen sampling, leukocyte trafficking, and adaptive immune activation [1] [2]. Situated along afferent and efferent lymphatic vessels, LNs regulate the movement of lymph and cells while providing stromal niches that organize immune cell interactions and tune responses to pathogens and vaccines.

The LN microanatomy creates distinct hydrodynamic and transport regimes. Lymph enters the subcapsular sinus (SCS), where lymphatic endothelial cells (LECs) and SCS macrophages capture and route cargo; in parallel, size-selective access to the fibroblastic reticular cell (FRC) conduit network partitions small solutes from larger complexes and cells, shaping antigen delivery and immune-cell localization [2] [3] [4]. These interfaces influence both protective immunity and disease progression.

Because many LN transport processes are difficult to measure across scales, computational models have become essential to probe node-scale hydraulics and mass transfer. Foundational and recent work consistently represent the SCS/medullary sinuses as free fluid regions coupled to a porous parenchyma (e.g., Darcy/Brinkman formulations), highlighting how geometry and permeability govern flow partitioning and pressure drop; notably, most lymph, on the order of >90% in a mouse LN model, traverses peripheral sinusoidal pathways with only a minority perfusing the core [5] [6] [7]. Reviews of lymphatic CFD underscore the need for integrated, validated models that connect flow, solute/cell transport, and tissue mechanics [8].

Parallel progress in lymphatic biomechanics shows that LN tissue properties remodel with inflammation, altering stiffness and potentially feeding back on transport. Such findings strengthen the rationale for models that incorporate not only free-flow and porous transport but also tissue mechanics (e.g., poroelasticity) to represent fluid–solid interactions under physiologic loading [9].

Validation remains a critical need. Residence-time distribution (RTD) analysis offers an interpretable, system-level metric that integrates geometry, permeability, and flow-partitioning effects on solute wash-in/wash-out dynamics. RTD methods, well established in transport reactor and membrane systems, provide a direct bridge between simulations that pulse a passive tracer and measurable effluent concentration histories, enabling calibration of hard to measure parameters such as medullary permeability [10] [11].

In this context, the present study formulates a two-dimensional LN model that links incompressible Navier–Stokes flow in sinusoidal free-fluid domains to Darcy/Brinkman transport in the porous

parenchyma, couples advection–diffusion of a passive solute (and cell surrogates), and includes poroelastic tissue mechanics to capture fluid–structure interactions. The model is implemented in a commercial finite-element framework, facilitating consistent treatment of interface conditions and material parameterization. Using an RTD protocol, the model is calibrated against pressure drop and effluent tracer dynamics, yielding quantitative readouts (e.g., shunting fractions, wall-shear ranges, mean residence time) that are relevant to immunoengineering and clinically pertinent contexts such as lymphedema and metastatic dissemination [12].

Theory / Experimental Set Up

Geometry

A 2D axisymmetric cross-section of a single LN was constructed manually, consisting of (i) a thin subcapsular sinus (SCS) contiguous with medullary sinus channels modelled as free-flow domains; (ii) a centrally located porous parenchymal core; and (iii) short afferent inlet segments and an efferent outlet segment modelled as free-flow ducts. The geometry mirrored prior image-guided and continuum descriptions that explicitly separate a peripheral sinusoidal pathway from a low-permeability core and thereby reproduced dominant peripheral shunting [5] [6] [7].

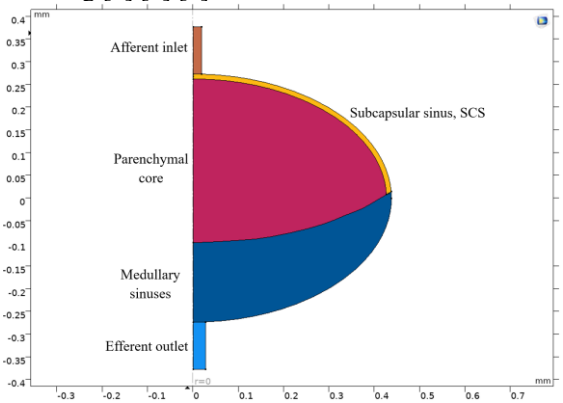

Figure 1: 2D Axisymmetric Lymph Node Geometry with Free-Flow Sinuses and Porous Core

Materials and porous properties

Lymph was modelled as an incompressible Newtonian fluid (density and viscosity within physiological ranges used in LN CFD studies), assigned uniformly to all free-flow regions [8]. The parenchyma was treated as a saturated porous medium with porosity ϕ and intrinsic permeability k. In keeping with the literature emphasizing restricted core perfusion and sensitive dependence of node-scale hydraulics on medullary properties, permeability in the sinus/medullary pathway was parameter-swept for calibration, while the deeper parenchyma used a lower baseline k [5] [7]. Where appropriate, effective diffusivity in porous domains reflected porosity/tortuosity adjustments to the free-solution diffusivity.

Boundary and initial conditions

A prescribed volumetric inflow Q_{in} was applied at the afferent inlet windows (equivalently, a uniform inlet velocity over each window), internal solid boundaries were no-slip, and the efferent outlet was set to a fixed static pressure with backflow suppression. These conditions were standard for lymph-node models that target the transnodal pressure drop Δp and the sinus–core flow partitioning [5] [6] [7]. The stationary hydraulic solution seeded the subsequent transport step.

For the residence-time distribution (RTD) analysis, a short top-hat tracer pulse $c_{in}(t)$ was imposed at the inlets on the stationary flow field; all walls were treated as no-flux, and the outlet used a convective-flux condition. The effluent signal was defined as $S(t) = C_{out}(t)Q_{out}(t)$, where $C_{out}(t)$ is the cross-sectional (or area-averaged) tracer concentration at the efferent outlet and $Q_{out}(t)$ is the volumetric efflux rate at that outlet. The total injected tracer mass is $M_{in} = \int_0^\infty c_{in}(t)Q_{in}(t)dt$, since the model has a single afferent inlet. (For a top-hat pulse of amplitude c_0 and duration Δt_p, this reduces to $M_{in} = c_0 \int_{pulse} Q_{in}(t)dt$.) The E-curve, cumulative distribution, and mean residence time were computed as $E(t) = \frac{S(t)}{M_{in}} = \frac{C_{out}(t)Q_{out}(t)}{M_{in}}$; $F(t) = \int_0^t E(\tau)d\tau$; $\bar{t} = \int_0^\infty tE(t)dt$, with $\int_0^\infty E(t)dt = 1$ [10]. This protocol provided a system-level observable that integrates geometry, permeability, and hydraulic partitioning.

Clinical and mechanistic context (for calibration choices)

Inflammation-driven remodelling altered stromal mechanics and could modulate intranodal hydraulics, which reinforced the inclusion of poroelastic effects in the setup and the use of RTD as a robust, system-level comparator [9] [10]. The chosen targets and parameterization were consistent with recent LN modelling studies and reviews [5] [6] [7] [8].

Governing Equations / Numerical Model / Simulation / Methods

Scope and physics

The lymph node (LN) section was modelled as a coupled free–porous domain with compliant tissue. Free-flow regions (subcapsular/medullary sinuses

and short duct segments) were governed by the incompressible Navier–Stokes equations (Laminar Flow). The parenchymal core was treated with Darcy/Brinkman theory for superficial velocity. Solute (and cell surrogate) transport followed advection–diffusion (Transport of Diluted Species). Tissue deformation–pore pressure coupling was represented with linear Biot poroelasticity via the Poroelasticity multiphysics node. These pairwise couplings were taken from predefined COMSOL Multiphysics interfaces (Free and Porous Media Flow; Poroelasticity), ensuring consistent continuity at free/porous interfaces and bidirectional coupling of pore pressure and solid strain. This stack aligned with recent LN modelling practice [6] [7] [8].

Governing equations

1. **Free-flow (sinuses and short ducts)**

Incompressible Navier–Stokes (Laminar Flow) was used; at LN scales, the Stokes limit applied where inertia was negligible [13]:

$$\rho\left(\frac{\partial \mathbf{u}}{\partial t}+\mathbf{u}\cdot\nabla\mathbf{u}\right)=-\nabla p+\mu\nabla^2\mathbf{u}$$
$$\nabla\cdot\mathbf{u}=0$$

where $\mathbf{u}$ is fluid velocity [m·s^{-1}], p pressure [Pa], ρ fluid density [kg·m^{-3}], and μ dynamic viscosity [Pa·s].

Stokes limit (low-Re):

$$-\nabla p+\mu\nabla^2\mathbf{u}=0$$

2. **Porous flow (parenchyma)**

The porous core used Darcy's law with mass conservation; near interfaces a Brinkman correction was available to include viscous shear [14]:

$$\mathbf{u}=-\frac{\kappa}{\mu}(\nabla p-\rho\mathbf{g})$$

where κ is intrinsic permeability [m^2] and $\mathbf{g}$ gravitational acceleration [m·s^{-2}].

Brinkman transition (when shear within the pores was non-negligible):

$$-\nabla p+\mu\nabla^2\mathbf{u}-\frac{\mu}{\kappa}\mathbf{u}+p\mathbf{g}=0$$

in which $\frac{\mu}{\kappa}\mathbf{u}$ is the Darcy drag term.

3. **Poroelastic tissue (Biot theory)**

Pore pressure p, solid displacement $\mathbf{u}_s$, and Darcy flux $\mathbf{q}$ were coupled by linear Biot poroelasticity [15] [16]:

$$\nabla\cdot\boldsymbol{\sigma}'-\alpha\nabla p+\rho_s\mathbf{b}=0$$
$$S\frac{\partial p}{\partial t}+\alpha\frac{\partial}{\partial t}(\nabla\cdot\mathbf{u}_s)+\nabla\cdot\mathbf{u}=0$$

where $\boldsymbol{\sigma}'$ is the effective stress tensor [Pa], α the Biot coefficient, S specific storage [Pa^{-1}], $\mathbf{u}_s$ solid displacement [m], $\mathbf{u}$ Darcy flux [m·s^{-1}], ρ_s solid density [kg·m^{-3}], and $\mathbf{b}$ body-force acceleration (e.g., $\mathbf{g}$) [m·s^{-2}].

4. **Solute (tracer) transport in free and porous regions**

Advection–diffusion was solved in both regions; porous media used an accumulation term with porosity ϕ and an effective diffusivity D_{eff} (volume-averaged/tortuosity-corrected) [17]:

$$\frac{\partial(\varepsilon c)}{\partial t}+\nabla\cdot(\mathbf{u}c)=\nabla\cdot\left(\varepsilon D_{eff}\nabla c\right)+R(c)$$

with ε=1 in free flow and $\varepsilon=\phi$ in porous media, and $R(c)$=0 for a nonreactive tracer. Here c is concentration [mol·m^{-3}], D_{eff} effective diffusion coefficient [m^2·s^{-1}], ε void fraction, and ϕ porosity.

Interface conditions and couplings

At free/porous interfaces, continuity of normal mass flux and traction/pressure compatibility were enforced. For transported species, continuity of concentration and advective–diffusive flux was imposed with no interfacial storage. Poroelastic coupling used the linear Biot formulation in the quasi-static limit, linking Darcy flux to solid equilibrium through Biot's coefficient α and specific storage S.

Numerical model and discretization

The previously defined 2D axisymmetric domain was discretized with equal-order finite elements with built-in stabilization where required by the governing equations. The stationary hydraulic problem (Stokes–Darcy/Brinkman, with optional poroelastic coupling) was solved first and supplied initial conditions for the subsequent transient tracer-transport step. Algebraic convergence for the stationary solve was judged by residual norms and interface-flux continuity to prescribed solver tolerances. A single mesh was used for both the stationary and transient solves.

Mesh and verification

The axisymmetric domain was meshed with unstructured triangular elements. Boundary-layer rows were placed along the capsule/subcapsular sinus and the afferent/efferent ducts to resolve near-wall shear, and element sizes were graded across sinus–parenchyma interfaces to preserve velocity and flux continuity. Three systematically refined meshes (M1–M3) were generated with near-interface growth ≤1.1 and ≥3 boundary-layer rows in free-flow regions. The same mesh was used for the transient transport simulations; no remeshing was required.

Mesh independence was assessed by tracking (i) transnodal pressure drop Δp, (ii) integrated outlet flux Q_{out}, (iii) peripheral shunting fraction, and (iv) the first moment of the residence-time distribution (mean RTD). Refinement from M2 to M3 changed Δp by <1%, Q_{out} by <0.1%, shunting by <0.5 percentage points, and mean RTD by <2%; M2 was therefore taken as sufficient resolution. In advection-

dominated zones, the consistent streamline-diffusion stabilization was used, and cell Péclet numbers were monitored to remain within an acceptable range.

Post-processing (RTD)
Using the RTD definitions introduced in the Introduction, global variables and integration boundaries were set in COMSOL to compute the inlet tracer mass M_{in} and the outlet RTD signal $E(t)$ (time in hours; E reported in h^{-1}). The mean residence time τ was obtained by global time integration of $t\,E(t)$. The $\{t,E(t)\}$ series was exported to MATLAB for cumulative trapezoidal integration to produce $F(t)$; the mass-recovery check $\int E(t)\,dt \approx 1$ was verified [10].

Studies and parameter sweeps
A stationary study performed a parametric sweep over medullary/sinus permeability k (and, if needed, porosity or outlet pressure) to match literature-anchored targets (node-scale Δp on the order of ~mmHg and dominant peripheral shunting), consistent with LN modelling that predicts >90% peripheral flow in mouse [5] [6] [7]. The validated operating point then seeded the transient transport run for RTD metrics.

Experimental Results / Simulation Results / Discussion

Validation strategy and observables
Analyses focused on node-scale pressure drop (Δp), flow partition between the peripheral subcapsular/medullary pathway and porous core, velocity and wall shear distributions, interstitial pressure levels, and tracer-based residence-time distribution (RTD). Post-processing definitions (area-weighted inlet/outlet pressures, internal control-surface fluxes, capsule shear sampling, and RTD construction from $C_{out}(t)Q_{out}(t)$ were specified a priori.

Transnodal pressure drop
At the calibrated operating point $k_{MS}=4.85\times10^{-13}$ m^2 and $Q_{in}=0.01$ mL·h^{-1}, the area-weighted transnodal drop was $\Delta p \approx 133.8$ Pa (1.004mmHg) with inlet and outlet pressures of 600.48 Pa and 466.64 Pa, respectively. This matched the a priori ~1 mmHg validation target drawn from murine LN modelling that reported a hydrostatic loss of "approximately 1 mmHg across the entire lymph node" [5]. For physiological context, classic perfusion data support a measurable node resistance/pressure drop that scales with flow [18].

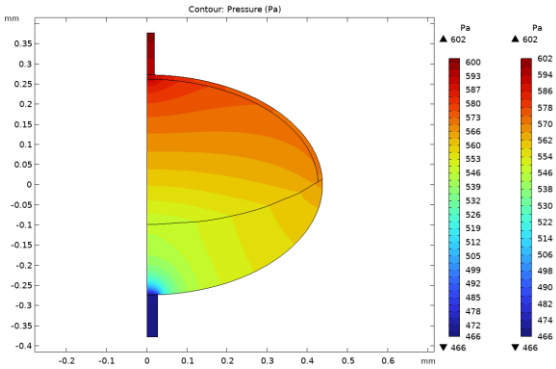

Figure 2: Pressure field and transnodal pressure drop (Δp ≈ 1.00 mmHg).

Mass conservation
A global continuity check gave $Q_{in}=Q_{out}=2.7778\times10^{-12}$ m^3·s^{-1} and $(Q_{in}-Q_{out})/Q_{in}=0\%$, confirming numerical balance for the reported solutions.

Flow partition (peripheral shunting)
Control-surface fluxes indicated that 99.9% of lymph exited via the peripheral SCS/medullary pathway, with only a minor fraction entering the parenchymal core. This near-unity shunting is directionally consistent with prior modelling that reported about 90% peripheral routing [5]; that study coupled flow to absorption by parenchymal blood vessels, which increases core perfusion and can lower the peripheral fraction relative to the present parameterization. An independent spherical-node analysis likewise reports >90% peripheral routing [19].

Velocity and wall shear fields
The SCS centreline velocity peaked at ≈5–6 mm·min^{-1} immediately downstream of the afferent entry and decayed to <0.5 mm·min^{-1} near the hilum; the arc-length-averaged centreline speed (excluding the inlet/outlet windows) was ≈0.5–0.6 mm·min^{-1} (Figure 3). Capsule/SCS wall-shear stress averaged 0.124 Pa (1.24 dyn·cm^{-2}) on the capsule ceiling and 0.104 Pa (1.04 dyn·cm^{-2}) on the floor, with a localized maximum of 1.246 Pa (12.5 dyn·cm^{-2}) near the afferent entry (Figure 4). For validation context, literature places entry-region SCS speeds on the order of 1–10 mm·min^{-1} with downstream decay, and lymphatic endothelial shear broadly in the ~0.1–10 dyn·cm^{-2} range, with higher local peaks under inflammatory remodelling [5] [20] [21].

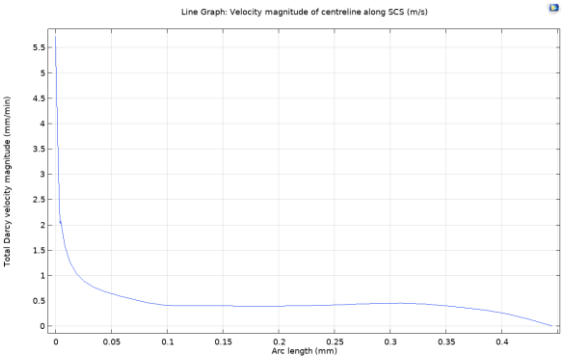

Figure 3: SCS centreline velocity vs. arc length (mm·min⁻¹). Arc length s was measured along the capsule/SCS midline from the afferent entry (s=0) toward the hilum; the centreline was sampled at the SCS mid-thickness.

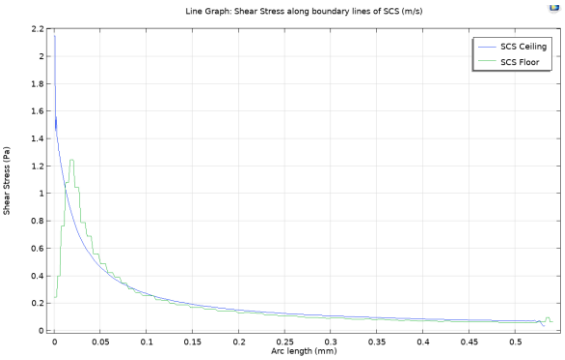

Figure 4: Capsule/SCS wall shear stress vs. arc length (Pa; ceiling & floor)

Interstitial pressure levels

The mean intranodal (porous-domain) pressure was 561.9 Pa (4.215 mmHg), with a spatial range of 3.500–4.459 mmHg. For validation, in-vivo measurements in mouse popliteal LNs report absolute intranodal pressures ≈ 5 mmHg [22]. Given the imposed efferent outlet of 3.5 mmHg and a calibrated node-scale drop of ≈ 1 mmHg, the expected field is ~3.5–4.5 mmHg, which matched the distribution observed here. This absolute scale is also consistent with contemporary LN hydraulic models that reproduce mmHg-level drops under physiological throughputs [5] [7].

Species transport transients (T cells, B cells, other leukocytes)

Species transport reflected the hydraulic partition. After a step input at the afferent, concentrations along the SCS rose rapidly and then equilibrated, while penetration into the porous core lagged. Volume-averaged transients showed t_{95} values of ~2–4 min (T cells) and ~6–8 min (Other, B cells), consistent with fast peripheral advection followed by slower exchange with the parenchyma (Figure 6). Spatial maps at 60 s and 600 s (Figure 5) revealed near-uniform filling of the SCS by 10 min with persistent gradients toward the core.

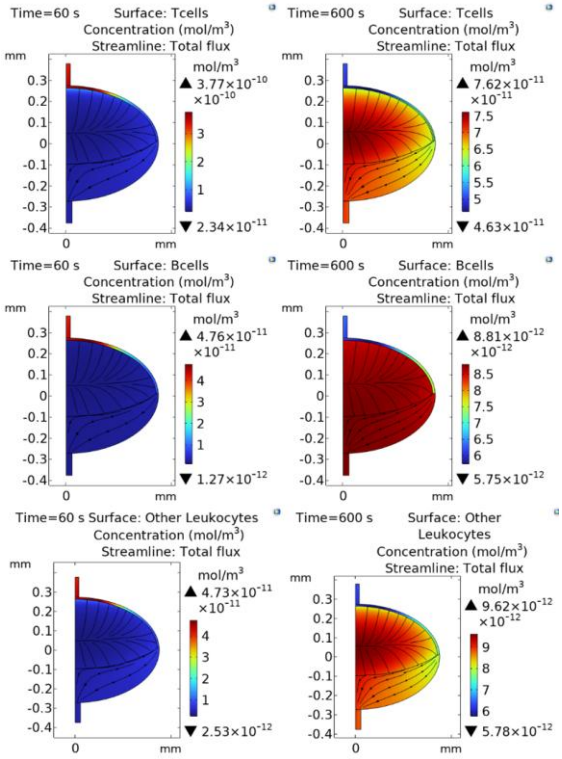

Figure 5: Species concentration snapshots (T cells, B cells, Other) at 60 s and 600 s (with streamlines)

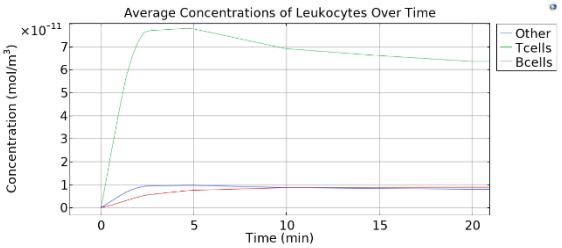

Figure 6: Volume-averaged species concentration vs. time (0–20 min)

Tracer RTD and mean residence time

Following a 10-s tracer pulse, the cumulative distribution F(t) rose sharply within the first hour, indicating rapid clearance through the peripheral SCS/medullary pathway (Figure 8). By ~2–3 h, F(t) exceeded 0.9; thereafter the curve flattened and approached unity by ~4–5 h, confirming near-complete mass recovery. The long late-time tail was consistent with slower exchange/retention in the parenchymal core, as also evident in the RTD density $E(t)$ (Figure 7). The mean residence time was $\tau \approx 14{,}310$ s (3 h 58 min 30 s). These features were consistent with LN tracer wash-in/wash-out

behaviour reported experimentally [23].

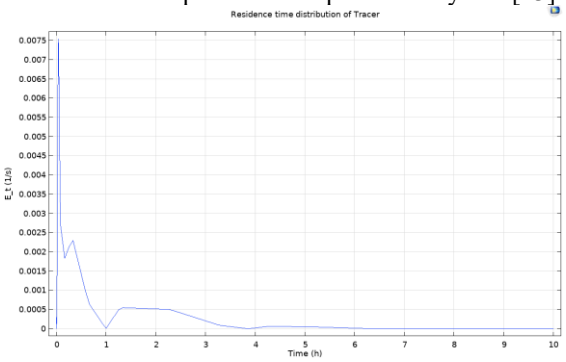

Figure 7: Residence-time distribution E(t) after a 10-s tracer pulse

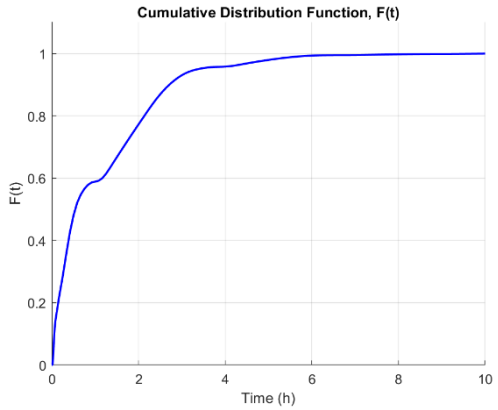

Figure 8: Cumulative distribution F(t) (with mean residence time τ)

Sensitivity to medullary permeability

A sweep over $k_{MS} \in [1.7\times10^{-13}, 1.7\times10^{-12}]$ m^2 produced the expected monotonic inverse relation between Δp and permeability; e.g., $\Delta p \approx 2.317$ mmHg at 1.7×10^{-13} m^2, 1.31 mmHg at 3.4×10^{-13} m^2, 0.968 mmHg at 5.1×10^{-13} m^2, decreasing to 0.477 mmHg at 1.7×10^{-12} m^2. The selected $k_{MS}=4.85\times10^{-13}$ m^2 placed Δp in the ~1 mmHg window while maintaining plausible shear and core velocities.

Synthesis and interpretation

The triad of ~1 mmHg node scale drop, near unity peripheral routing, and long tailed RTD supports a picture in which geometry and permeability, not large pressure gradients, govern partitioning: rapid SCS/medullary advection clears most inflow, while a minority exchanges with the low permeability core and exits slowly. This pattern is consistent with image-based and multiscale LN analyses [5] [7].

Limitations

Results were obtained in 2D axisymmetry with steady hydraulics feeding transient transport; valves, pulsatility, and microvascular exchange were not explicitly resolved. These simplifications can accentuate peripheral shunting and narrow the pressure band; future work may incorporate pulsatile driving and explicit vascular exchange to test robustness.

Conclusions

This study developed and calibrated a 2D axisymmetric lymph-node model coupling Stokes flow in the subcapsular/medullary sinuses and short ducts to Darcy flow in a porous parenchyma, with optional Biot poroelasticity. With $Q_{in}=0.01$ mL·h^{-1} and $p_{out}=3.5$ mmHg, the model reproduced a transnodal pressure drop near 1 mmHg, yielded overwhelmingly peripheral flow partition, and provided quantitative shear, interstitial pressure, and RTD metrics suitable for validation.

Key outcomes were as follows: (i) $\Delta p \approx 1.00$ mmHg at the calibrated $k_{MS}=4.85\times10^{-13}$ m^2; (ii) peripheral shunting of ~99.9%; (iii) SCS centreline velocity peaked at ~5–6 mm·min^{-1} near the afferent and fell to <0.5 mm·min^{-1} toward the hilum (mean ~0.5–0.6 mm·min^{-1}); wall shear averaged ~0.12/0.10 Pa (ceiling/floor) with a local maximum ~1.25 Pa near the inlet; (iv) interstitial (parenchymal) pressure confined to 3.5–4.46 mmHg (mean 4.22 mmHg); (v) global mass-balance error ~0%; and (vi) RTD mean ≈3 h 58 min, with a fast peripheral lobe and a long tail from slow core exchange.

Parametric analysis demonstrated a strong, monotonic sensitivity of Δp to k_{MS} over 1.7×10^{-13}–1.7×10^{-12} m^2, providing a clear calibration handle to match physiologic pressure drops while maintaining plausible shear and velocity fields. Together, these results support a hydraulically driven picture in which node geometry and permeability, rather than large pressure gradients, govern partitioning between rapid sinusoidal advection and slower core exchange.

The calibrated baseline established here is well positioned for mechanistic extensions: transient/pulsatile inflow and valve dynamics, explicit blood–lymph exchange, spatial heterogeneity in porosity/permeability and stiffness, chemokine-guided species transport with receptor–ligand kinetics, and 3D geometries. These additions would enable deeper interrogation of immune-cell residence, antigen exposure histories, and therapeutic strategies that rely on lymph-borne delivery.

References

[1] M. J. Davis, S. D. Zawieja and P. D. King, "Transport and Immune Functions of the Lymphatic System," *Annual Review of Physiology,* vol. 87, no. 1, p. 151–172, 2025.

[2] L. Li, J. Wu, R. Abdi, C. M. Jewell and J. S. Bromberg, "Lymph Node Fibroblastic Reticular Cells Steer Immune Responses," *Trends in Immunology,* vol. 42, no. 8, p. 723–734, 2021.

[3] A. Takeda, M. Salmi and S. Jalkanen, "Lymph Node Lymphatic Endothelial Cells as Multifaceted Gatekeepers in the Immune System," *Trends in Immunology,* vol. 44, no. 1, p. 72–86, 2023.

[4] K. Maisel, C. A. McClain, A. Bogseth and S. N. Thomas, "Nanotechnologies for Physiology-Informed Drug Delivery to the Lymphatic System," *Annual Review of Biomedical Engineering,* vol. 25, p. 233–256, 2023.

[5] M. Jafarnejad, M. R. Woodruff, P. S. Zawieja, J. B. Carroll and J. E. J. Moore, "Modeling Lymph Flow and Fluid Exchange with Blood Vessels in Lymph Nodes," *Lymphatic Research and Biology,* vol. 13, no. 4, p. 234–247, 2015.

[6] G. Giantesio, A. Girelli and A. Musesti, "A Model of the Pulsatile Fluid Flow in the Lymph Node," *Mechanics Research Communications,* vol. 116, p. 103743, 2021.

[7] A. Girelli, G. Giantesio, A. Musesti and R. Penta, "Multiscale Computational Analysis of the Steady Fluid Flow through a Lymph Node," *Biomechanics and Modeling in Mechanobiology,* vol. 23, p. 2005–2023, 2024.

[8] T. D. Jayathungage Don, S. Safaei, G. D. Maso Talou, P. S. Russell, A. R. J. Phillips and H. M. Reynolds, "Computational Fluid Dynamic Modeling of the Lymphatic System: A Review of Existing Models and Future Directions," *Biomechanics and Modeling in Mechanobiology,* vol. 23, no. 1, p. 3–22, 2024.

[9] F. P. Assen, J. Abe, M. Hons, R. Hauschild, S. Shamipour, W. A. Kaufmann, T. Costanzo and e. al., "Multitier Mechanics Control Stromal Adaptations in Swelling Lymph Nodes," *Nature Immunology,* vol. 23, no. 8, p. 1246–1255, 2022.

[10] A. E. Rodrigues, "Residence time distribution (RTD) revisited," *Chemical Engineering Science,* vol. 230, p. 116188, 2021.

[11] M. Hwang, J. Wang and S. Jung, "Understanding the Residence Time Distribution in a Transient Inline Spiking System: Modeling, Experiments, and Simulations," *Membranes,* vol. 13, p. 375, 2023.

[12] L. C. Dieterich, C. Tacconi, L. Ducoli and M. Detmar, "Lymphatic vessels in cancer," *Physiological Reviews,* vol. 102, no. 4, p. 1837–1879, 2022.

[13] R. L. Panton, Incompressible Flow, Hoboken, NJ: Wiley, 2013.

[14] D. A. Nield and A. Bejan, Convection in Porous Media, Cham: Springer, 2017.

[15] O. Coussy, Poromechanics, Hoboken, NJ: Wiley, 2004.

[16] A. H.-D. Cheng, Poroelasticity, Cham: Springer, 2016.

[17] M. Dentz, J. J. Hidalgo and D. Lester, "Mixing in Porous Media: Concepts and Approaches Across Scales," *Transport in Porous Media,* vol. 146, no. 1, p. 5–53, 2023.

[18] N. L. Browse, R. L. Doig and D. Sizeland, "The Resistance of a Lymph Node to Lymph Flow," *British Journal of Surgery,* vol. 71, no. 3, p. 192–196, 1984.

[19] G. Giantesio, A. Girelli and A. Musesti, "A Mathematical Description of the Flow in a Spherical Lymph Node," *Bulletin of Mathematical Biology,* vol. 84, p. 142, 2022.

[20] J. A. Kornuta, Z. Nepiyushchikh, O. Y. Gasheva, A. Mukherjee, D. C. Zawieja and J. B. Dixon, "Effects of dynamic shear and transmural pressure on wall shear stress sensitivity in collecting lymphatic vessels," *American Journal of Physiology–Regulatory, Integrative and Comparative Physiology,* vol. 309, no. 9, p. R1122–R1134, 2015.

[21] J. E. J. Moore and C. D. Bertram, "Lymphatic System Flows," *Annual Review of Fluid Mechanics,* vol. 50, no. 1, p. 459–482, 2018.

[22] E. M. Bouta, R. W. Wood, E. B. Brown, H. Rahimi, C. T. Ritchlin and E. M. Schwarz, "In vivo quantification of lymph viscosity and pressure in lymphatic vessels and draining lymph nodes of arthritic joints in mice," *The Journal of Physiology,* vol. 592, no. 6, pp. 1213-1223, 2014.

[23] C. C. Clement, W. Wang, M. Dzieciatkowska, M. Cortese, K. C. Hansen, A. Becerra, S. Thangaswamy, I. Nizamutdinova, J.-Y. Moon, L. J. Stern, A. A. Gashev, D. Zawieja and L. Santambrogio, "Quantitative Profiling of the Lymph Node Clearance Capacity," *Scientific Reports,* vol. 8, no. 1, p. 11253, 2018.

Appendix

***Table 1**: Baseline model inputs and sweep ranges for the axisymmetric lymph node simulations (geometry, materials, boundary conditions, and transport).*

Category	Quantity	Symbol	Baseline	Units
Geometry (axisymmetric)	Outer ellipse semi-axis (radial)	a_{out}	0.80	mm
	Outer ellipse semi-axis (axial)	b_{out}	0.50	mm
	SCS inner ellipse semi-axis (radial)	$a_{SCS,in}$	0.79	mm
	SCS inner ellipse semi-axis (axial)	$b_{SCS,in}$	0.49	mm
	Parenchyma ellipse semi-axis (radial)	a_{core}	0.78	mm
	Parenchyma ellipse semi-axis (axial)	b_{core}	0.48	mm
	SCS nominal thickness (radial/axial)	t_{SCS}	0.01	mm
	Afferent window width	w_{aff}	0.07	mm
	Afferent window height	h_{aff}	0.20	mm
	Efferent window width	w_{eff}	0.10	mm
	Efferent window height	h_{eff}	0.20	mm
Fluid (free-flow: SCS/EF/AF)	Density	ρ	1040	$kg \cdot m^{-3}$
	Dynamic viscosity	μ	1.2×10^{-3}	$Pa \cdot s$
Fluid in porous regions (Darcy)	Density	ρ	1000	$kg \cdot m^{-3}$
	Dynamic viscosity	μ	1.2×10^{-3}	$Pa \cdot s$
Porous matrix - TC (parenchyma)	Porosity	Φ	0.30	—
	Intrinsic permeability	κ	7.6×10^{-17}	m^2
	Young's modulus (drained)	E	2×10^{3}	Pa
	Poisson's ratio	ν	0.35	—
Porous matrix — MS (medullary)	Porosity	Φ	0.65	—
	Intrinsic permeability	κ	4.85×10^{-13}	m^2
	Young's modulus (drained)	E	1200	Pa
	Poisson's ratio	ν	0.35	—
Poroelastic coupling	Biot–Willis coefficient	α_B	0.8	—
Free-flow BCs	Inlet (afferent)	—	2.7778×10^{-12}	$m^3 \cdot s^{-1}$
	Outlet pressure (efferent)	p_{out}	466.6	Pa
Species (solutes)	Diffusivity — small tracer	D_{small}	4.6×10^{-10}	$m^2 \cdot s^{-1}$
Species (cells)	Fluid diffusion — T cells	D_T	1.1×10^{-12} (≈67 μm²/min)	$m^2 \cdot s^{-1}$ (μm²/min)
	Fluid diffusion — B cells	D_B	2.0×10^{-13} (≈12 μm²/min)	$m^2 \cdot s^{-1}$ (μm²/min)
	Fluid diffusion — other leukocytes (non-B, non-T; e.g., NK, dendritic)	D_{other}	5.0×10^{-13} (≈30 μm²/min)	$m^2 \cdot s^{-1}$ (μm²/min)
	Concentration — T cells	c_T	6.64×10^{-11}	$mol \cdot m^{-3}$
	Concentration — B cells	c_B	8.3×10^{-12}	$mol \cdot m^{-3}$
	Concentration — other leukocytes (non-B, non-T)	c_{other}	8.3×10^{-12}	$mol \cdot m^{-3}$
Axisymmetry	Swirl velocity	u_θ	0	—
RTD (transient tracer)	Pulse duration	t_p	10	s
	Pulse magnitude	c_0	8.3×10^{-12}	$mol \cdot m^{-3}$